HIGH SCHOOL EDITION
Journal of Student Research
Volume 10 Issue 4 (2021)

Quantitative Comparison of a Hierarchy of Commonly Used Planetary Climate Energy Balance Models

Mihir Dasgupta[1] and Joy Merwin Monteiro[2]

[1]Greenwood High International School, Bangalore, Karnataka, India
[2]Advisor, Indian Institute of Science Education and Research, Pune, Maharashtra, India

ABSTRACT

The objective of this paper is to examine the effect of the various simplifications inherent in commonly used planetary energy balance climate models (EBMs). Specifically, we look at the zero-dimensional (0-d) radiative equilibrium model, the 1-d radiative equilibrium model, and the 1-d radiative-convective equilibrium (RCE) model. Each of these models make fundamental steps towards a well-represented Earth system model, and make different simplifications and assumptions in the process. We seek to evaluate the effects these assumptions have on key thermal quantities of the system (OLR / outgoing longwave radiation, surface temperature, etc.). These evaluations lead us to identify contexts for each model wherein it remains a valid option to accurately replicate a system. The 0-d model fails to account for the greenhouse effect's impact on energetics, thus predicting an erroneously-low surface temperature and low OLR. It instead requires an emissivity coefficient ~ 0.619 to balance OLR and temperature and model the Earth system. The 1-d radiative equilibrium model is a significant improvement on its predecessor, creating a stratospheric thermal profile reasonably similar to that of the Earth. The strong low-altitude temperature lapse rate and convective instability near the surface, however, slightly diminishes the validity of the low-level thermal profile – a drawback the RCE model appears to resolve with the addition of convective and boundary layer components. We conclude that the 0-d radiative equilibrium is best suited to isothermal atmospheres, the 1-d radiative equilibrium model to non-isothermal atmospheres where convection is suppressed, and the 1-d RCE model to convectively active atmospheres.

Introduction

Climate modeling is a fundamental method used to help both our understanding of past climate states and predicting future states through various forcing techniques. It has become a significant tool in climate science because of the environment they provide researchers with: one in which they can perform large-scale experiments and draw meaningful conclusions. The core of their effectiveness arguably lies in their examination of the energetics of the system. Dynamics prevalent in the atmospheric and oceanic circulatory systems are results of energy imbalances, as methods to bring the system to thermal equilibrium. Therefore, a flawed interpretation of the energy budget potentially disables evaluations of any other dynamics derived from its results. Energy balance models (EBMs) attempt to determine key quantities of a planetary system (e.g., radiative flux profiles, air temperature, optical depth, surface temperature) without resolving the dynamics that arise due to resulting energetic imbalances. Therefore, they may be considered a precursor to a general circulation model (GCM), in that they quantify the energy gradients from which dynamics are derived.

Given that these models attempt to study climate, it is imperative that the system remain in a statistically steady state. While model variables may be subject to change, the system's statistics - the mean and variance for instance - must remain constant. If a system meets this criterion, we claim it has reached equilibrium. Our method to evaluate equilibrium rests on the premise of a balanced energy budget that accounts for both the energy input to and output from the system. An imbalance in the budget would ultimately lead to the complete vaporization or freezing of the planet. A predictable climate, and even the plausibility of habitability and the evolution of life, rest on this stability.

This paper uses OLR and surface temperature as performance indicators for each model. These are compared to climatologically normal observations (CNs) of the same. The models created are implemented in Python, primarily using the sympl library and the climt Earth system modeling toolkit (Monteiro et. al., 2018). The former provides a user with a framework which can be used to set up state dictionaries that track the evolution of key variables with the numerical integration of the time variable, largely through the Adams-Bashforth time-differencing technique (Durran, 1991). On the other hand, climt provides a set of 'components' that each model a given physical process in the system. These components can be used both independently, or in conjunction with others. The source code for the models we developed can be found on this GitHub repository (Dasgupta, 2021).

The NCEP/NCAR data (Kalnay et. al., 1996) we use to make an OLR estimation is reanalysis data. Reanalysis, short for retrospective analysis, relies on data assimilation in a suitable weather or climate model to provide an accurate estimate of the state of the atmosphere-ocean system. Data assimilation incorporates observations of certain variables to guide or nudge the model in the correct direction. Broadly, reanalysis products aim to maintain and develop a record of how atmospheric quantities and conditions are changing over decades. The object of long-term reanalysis is to constantly improve existing estimates of the past state of the atmosphere and ocean. One could make the argument that using older remote sensing data could hamper the model due to its assumed unreliability. Furthermore, there is little to no centralized quality control maintained across data sources (satellites, ground-based stations, etc.). The grey area associated with addressing this concern led to the development of various reanalysis methodologies: e.g., ERA5 — from the European Centre for Medium Range Weather Forecasting (Hersbach et. al., 2020), JRA-55 — from the Japanese Meteorological Agency (Kobayashi et al., 2015), MERRA — from NASA / North American Space Agency (Gelaro et. al., 2017), etc.

This paper begins with an evaluation of the energy sources and sinks that impact the climate system (limited to the atmosphere and lithosphere) in order to focus the scope of our models' setups. The following section describes all 3 models that we seek to compare here, including the details of the equations, variables, and dynamics that govern them. We first discuss the 0-d energy balance model, with an emphasis on the abstractions made in order to reduce the Earth system to such an approximation. It is followed by an analysis of the two-stream Schwarzschild approximations and their influence on our 1-d models. We move on to describe their setup and initial conditions. The 'Results' section discusses the output values and profiles for the 3 models. We close with a discussion on the contexts for which each of the three models are best suited and a description of the limitations of this study.

Methods And Methodology

Identifying Energy Sources & Sinks

Our first step in setting up the system constraints is in identifying the energy sources (provides energy) and sinks (removes energy) that drive the models. The importance of clearly identifying sources and sinks is paramount. By understanding the mechanisms by which energy is gained or lost from the system, we understand the stability of the system. It rests on the premise of a balanced energy budget (where there is no net energy input or output to or from the system). We begin with an evaluation of potential energy sources.

The concentration of matter at the Earth's core creates heat because of its displacement towards the planet's gravitational core (Ernst et al., 2016): the conversion of gravitational potential to thermal energy occurs as the distance between the observed matter and the Earth's core falls. The collapse of matter during the formation of the planet released this energy as high levels of heat. This energy release drives an internal circulation underneath the Earth's crust. Therefore, any emitted energy as a result of cooling, sinking matter was transferred to the upward displacement of matter rising from the core - reflected by an increase in gravitational potential. The system forms a closed circulation that, today, does not significantly affect surface dynamics or temperatures. As a result, we can assume its influence on the Earth's energy budget is negligible and disregard its impact on this scope of discussion. The decay of

radioactive heavy metals in the Earth's inner core releases high levels of energy that serve as one of the main energy sources of the Earth's interior's dynamics. However, its impact on surface heating is dwarfed by that of insolation and is ignored in all 3 model setups.

The impact of solar and lunar tides can cause heating in the climate system. Their gravitational forces exerted on the Earth (and vice-versa) induce tidal bulges as the Earth system is distorted (e.g., oceanic tides). These bulges act as friction to the Earth's rotation, reducing its torque (Camuffo, 2001). The energy lost in rotation is converted to thermal energy in the asthenosphere. However, the crust acts as an insulator to the effects of both tidal friction and radioactive decay (Lenardic et al., 2005). It follows that these effects are often negligible on most other terrestrial planets as well. Therefore, the crust's presence reduces the influence of the internal energy dynamics of the Earth on the climate system - we can ignore their influences on the Earth's energy budget as we did the circulation of matter in the Earth's interior.

A remaining source of interest is incoming solar radiation, or insolation for short. The Sun remains the largest energy source on the Earth's climate system as it exists today. Given that the scope of observation is effectively limited to the surface, insolation is the only significant energy source worth accounting for in our model setups. Thus, the following models will consider only insolation an energy source to maintain their inherent simplicity.

We now concern ourselves with identifying the energy sink(s) in the system i.e., the mechanism(s) by which the system lose(s) energy. As the Earth's interior acts as a source of energy, it follows that it cannot act as a sink. This narrows our focus to the mechanisms that allow the system to lose energy outside the planetary body. One possibility is the loss of kinetic energy by the removal of matter from the system. Focusing on the Earth, this mass could be lost from particles in the atmosphere, more likely than anything else. However, the loss of matter from the atmosphere is negligible due to the strength of the Earth's gravitational field, derived from the planet's mass. The Earth's atmospheric escape primarily is due to losses in hydrogen (3 kg/s) and helium (50 g/s) via the Jeans escape, charge escape, and polar wind escape mechanisms (Catling & Zahnle, 2009). The other sink we can consider is the longwave radiation emitted from the Earth's surface. This acts as the primary energy sink in Earth's climate system and will be the only sink we consider in following models.

Threshold Climatological Normal (CN) Determination

Table 1. CN values of planetary albedo, surface temperature, and outgoing longwave radiation.

Quantity	CN Value
Albedo (α)	0.29
Surface Temperature (T)	$288.20 \pm 0.05\,K$ ($15.05 \pm 0.05\,°C$)
Outgoing Longwave Radiation (OLR)	234.17 W/m^2

The albedo coefficient accounts for the fraction of solar radiation incident on the Earth surface (insolation) that is reflected. We set $\alpha = 0.29$: a value consistent with accepted estimates of the Earth's current average albedo (Stephens et. al., 2015; Wielicki et. al., 1996; Jacobowitz & Tighe, 1984). We use GISS's 2020 estimate to set a surface temperature threshold: a (+1.05 ± 0.05) °C anomaly (Greene & Jacobs, NASA Release 21-005, 2021; Lenssen et. al., 2019) from the 1951-80 GISTEMP-4 baseline mean, which estimated a surface temperature of 14°C (Hansen et. al., 2010). Therefore, we set $T = 288.20 \pm 0.05\,K$ (15.05 ± 0.05 °C). The other thermal quantity considered in measuring model performance is planetary OLR. We use spatially- and temporally- interpolated OLR data provided by NOAA (Liebmann & Smith, 1996) to accomplish this. A global mean from 1991-2020 is taken to determine $OLR =$ 234.17 W/m^2. We use cosine-weighting along the latitudinal (y-) axis to account for the distortion caused by the projection of a spherical surface onto a 2d plane.

Model 1: The Zero-Dimensional (0-d) Radiative Equilibrium Model

The zero-dimensional model is the simplest member of the EBM family. It views the Earth as an arbitrary, singular point in space, as if observed from an infinite distance. In this case, our key abstraction is to ignore any spatial variation and remove all real coordinates from the x, y and z axes. This allows us to utilize the horizontal homogeneity assumption as in (Meador & Weaver, 1980). The absence of any points of observation across altitude leads us to ignore the interference of an atmosphere in our energy budget, which simplifies our calculations significantly. Additionally, we assume a surface with a uniform albedo value. This allows us to operate under a single emitting surface temperature. The only variables to account for are the energy incident on the surface and the energy it emits, as was explained in the previous section on energy sources and sinks. We can now set up an energy budget equation.

We expect albedo to vary with surface temperature, seeing as it is largely determined by ice/snow presence on our idealized aqua-planet, and is thus treated as a variable. Solar irradiance (solar energy flux density at the top of the atmosphere), S has been approximated to 1367.6 W/m^2 (Johnson, 1954), and is thus treated as a constant. Viewed from the Sun, the planetary surface appears as a disk with surface area πR^2, where R is the distance from the Earth to the Sun. Assuming the surface reflects a certain fraction (α) of insolation, we can model the total radiation incident on the surface by the expression, $\pi R2S\ (1\ -\ \alpha)$.

The Stefan-Boltzmann law provides us with a framework with which we can estimate Earth's emitted radiative flux given its emitting temperature - σT^4 - where T is the equilibrium surface temperature and σ is a constant of proportionality (the Stefan-Boltzmann constant) ~ 5.68 x 10^{-8} W/m^{2}K^4. In order to test whether Earth's emitted radiation matches that predicted by the Stefan-Boltzmann law, we introduce a dimensionless emissivity ratio coefficient, ε, where $0\ <\ \varepsilon\ <\ 1$, into the expression. Thus, it becomes a gray representation of the Earth system. The surface usually has an emissivity very close to 1, given that it is set by the ocean. A value $\varepsilon = 1$ reverts the graybody back to its initial blackbody state since all incident radiation is absorbed. Accounting for the surface area of a sphere ($4\pi R^2$), we model the aggregate emitted radiation from the surface as $4\pi R^2\varepsilon\sigma T^4$. Therefore, as per the conservation of energy, we have $\pi R^2 S\ (1\ -\ \alpha)\ =\ 4\pi R^2\varepsilon\sigma T^4$. Simplifying,

Equation 1: The 0-d model:

$$\frac{S}{4}(1-\alpha) = \varepsilon\sigma T^4$$

Equation (1) completes the 0-d model. It consists of 3 variables to be evaluated: Average planetary albedo (α), the emissivity (ε), and surface temperature (T). S is treated as a constant here. Ordered triplets for the 3 variables that satisfy the Equation (1) are examples of parameters of an equilibrium state system.

Model 2: The One-Dimensional (1-d) Radiative Equilibrium Model

We extend the 0-d model here with a vertical dimension, while preserving our previous horizontal homogeneity assumption. As such, it becomes a single-column model. The radiative equilibrium model uses electromagnetic radiation as the sole method of energy transfer, implying a statically stable atmosphere: no transfer through the physical movement of air parcels takes place. We use the climt's interface to the RRTM-G (Rapid Radiative Transfer Model for GCMs) scheme here. It discretizes both the longwave and shortwave spectra into pseudo-monochromatic bands (Mlawer et. al., 1997) and develops optical depth (τ) profiles using mole fraction data for atmospheric constituents with significant influence on radiative absorbance. The absorbers considered for both Models 2 and 3 are ozone, carbon dioxide, and water vapor. Figure 1 shows the ozone and carbon dioxide distributions that stay constant throughout the model's runtime.

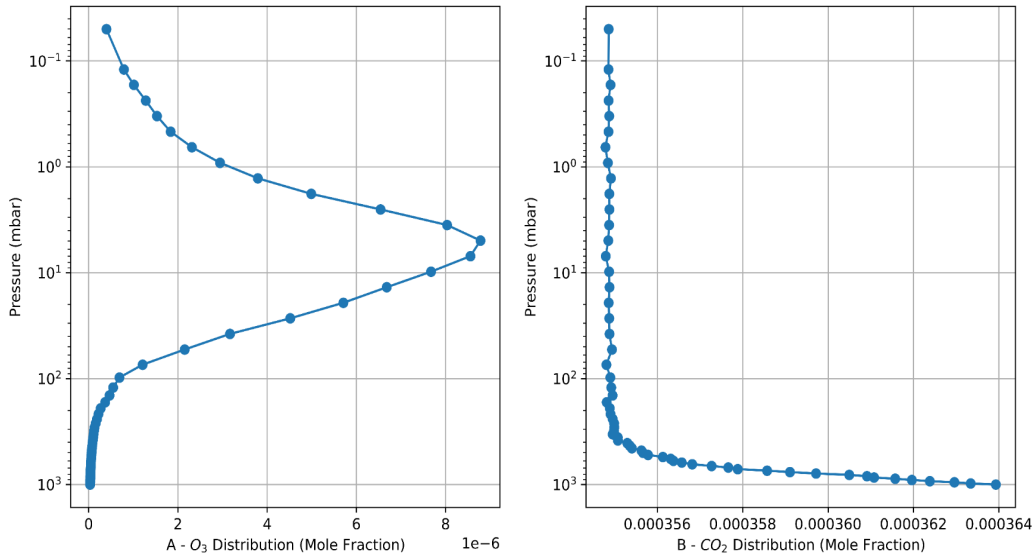

Figure 1. Mole fraction data for key absorbers. (1a) is the O_3 distribution, and (1b) is the CO_2 distribution.

We extend the 0-d model here with a vertical dimension, while preserving our previous horizontal homogeneity assumption. As such, it becomes a single-column model. The radiative equilibrium model uses electromagnetic radiation as the sole method of energy transfer, implying a statically-stable atmosphere: no transfer through the physical movement of air parcels takes place. We use the climt's interface to the RRTM-G (Rapid Radiative Transfer Model for GCMs) scheme here. It discretizes both the longwave and shortwave spectra into pseudo-monochromatic bands (Mlawer et. al., 1997) and develops optical depth (τ) profiles using mole fraction data for atmospheric constituents with significant influence on radiative absorbance. The absorbers considered for both Models 2 and 3 are ozone, carbon dioxide, and water vapor. Figure 1 shows the ozone and carbon dioxide distributions that stay constant throughout the model's runtime.

The Two-Stream Schwarzschild Approximations

Consider a 'slab' (of optical depth $\delta\tau$) of an atmosphere (with a finite number of layers) with a beam of intensity I incident on its lower surface. Note that optical depth is defined as the ratio of incident to transmitted radiant power through a material (McNaught, 1997) and thus is a measure of the slab's absorptive effects. Thus, the $\tau(z)$ functions express changes in optical depth and absorption throughout the atmosphere. The absorbed radiation can be modelled by the expression, $I\tau * \delta\tau$. This is the product of the radiative intensity, the absorptivity coefficient, and the slab depth, respectively. This sets up a conservation equation:

Equation 3: A conservation equation for the radiative transfer in 1-d models.

$$I\tau_*\delta\tau = (1 - \delta\tau_*)I + B\delta\tau_*$$

Where $(1 - \delta\tau_*)I$ is the fraction of unabsorbed radiation passing through the slab and B is the blackbody radiation emitted by the slab which is multiplied by $\delta\tau_*$ to define its final emitted radiative intensity. Calculating the net radiative up-flux involves integrating Eq. (2) for the full angular dependence of the flux. This is complicated by the inclusion of $cos\ \theta$ on the right-hand side and is thus estimated to the following approximations.

Equation 4: Differential forms of the Schwarzschild two-stream equations:

$$\frac{d}{d\tau_\nu} I_+ = -I_+ + \pi B(\nu, T(\tau_\nu))$$
$$\frac{d}{d\tau_\nu} I_- = I_- - \pi B(\nu, T(\tau_\nu))$$

Where I_+ and I_- are the upward and downward fluxes respectively. Separating the net flux equation into these two components gives rise to the two-stream Schwarzschild approximations.

To find functions for upwelling and downwelling radiative components, we convert these differential equations to their integral form. Since they are first-order ordinary differential equations, we use an integrating factor of $e^{-d\tau}$. Although the equations above describe flux as a function of frequency (ν), we replace them with monochrome functions for use in the RRTM-G scheme (given the discretized pseudo-monochromatic bands). It is assumed that the $\tau(z)$ function is adjusted for the different bands.

Equation 5: Integral form of the upwelling component of the Schwarzschild two-stream equations:

$$I_+(\tau) = I_+(0)\, e^{-\tau} + \int_0^\tau B(T(\tau))e^{-(\tau-\tau')}d\tau'$$

There are 2 sources shown here. The first term describes incident radiation from a level at $\tau = 0$ (the planet's surface). It is multiplied by an attenuation coefficient, $e^{-\tau}$, which accounts for the loss of flux intensity as the radiation passes through optically thick layers to reach the height τ. The second term integrates the emitted radiation from all levels between the surface and the observed height. This term also contains an attenuation coefficient ($e^{-(\tau-\tau')}$) that accounts for the loss in intensity between the observed and intermediate heights. The attenuation coefficients play a key role in determining the function's sensitivity to different layers' outputs.

Equation 6: Integral form of the downwelling component of the Schwarzschild two-stream equations:

$$I_-(\tau) = I_-(\tau_\infty)e^{-(\tau_\infty-\tau)} + \int_\tau^{\tau_\infty} B(T(\tau))e^{-(\tau-\tau')}d\tau'$$

The first term often carries a null value. This is because longwave radiation at the top of the atmosphere is not expected to be incident on the planet. The second term accounts for all downwelling back-radiation emitted by the atmosphere towards the surface. As seen in Equation 6, its attenuation coefficient increases radiative influence with τ' proximity to τ. The Schwarzschild equations indicate that OLR (defined as $I_+(\tau_\infty)$) is far more sensitive to upper-layer emission than surface- or lower- level emission, especially in the presence of gases that are strong longwave absorbers. This leads to large changes in optical depth over a unit distance and thus plays a key role in our interpretation of the 1-d models' output.

Planetary albedo is also estimated for all models because of its direct effect on OLR and surface temperature. We calculate planetary albedo as the ratio of the upwelling solar radiation at the top of the atmosphere to the solar energy input to the system, accounting for the average zenith angle.

Model Setup and Initial Conditions

This system consists of 2 physical components: an aquaplanet surface and an atmospheric column above it. The model's initial conditions are as follows: a surface temperature of 250 K, a vertically uniform air temperature of 230 K, and an ocean mixed layer depth of 40 m. We used a zenith angle of 75° and blocked any solar variation, maintaining a non-diurnal solar constant. The surface albedo setup used a direct shortwave albedo of 0.3, 0.3(sin π/3) for its diffuse

counterpart, and a value of 0.45 for near-infrared radiation. Note that the surface shortwave albedo is unlikely to exactly match the planetary shortwave albedo. This is caused by the absence of clouds in the model, which play a key role in setting planetary albedo. We do expect numerical errors when running the model, so we allow a small energy budget error margin of 0.5 W/m^2 in the stopping criterion.

Model 3: The One-Dimensional (1-d) Radiative-Convective Equilibrium (RCE) Model

The RCE model adds the option for convection to the base 1-d radiative equilibrium model. We accomplish this through a combination of the Emanuel convection scheme (Emanuel et. al., 1999) and a convective adjustment that prevents the temperature profile from remaining unstable. Both schemes are provided as climt components. Otherwise, the 1-d models are set up in a similar manner. The system is initialized with convective potential at all heights with moisture present. Our usage of convection as a modeling component is largely defined by (Manabe & Wetherald, 1967). Essentially, the RCE model is designed to account for any convective instability by employing convection as an adjustment mechanism to transport sufficient heat upwards when the temperature lapse rate passes a critical value of 6.5 C°km^{-1}. A boundary layer component is also added to allow sufficient heat transfer from the surface to the atmosphere. The model's initial surface conditions are identical to those of the 1-d radiative equilibrium model, except that the surface temperature is set to 275 K the air temperature is isothermalized to 250 K, and the surface albedo is set to 0.25. We use smaller (10-minute) time increments to make effective use of convection as an adjustment process.

Stopping Criteria: Models 2 and 3

Equation 7: A function for Models 2 and 3 that monitors the radiative flux (of all frequencies) entering (F_{IN}), or leaving (F_{OUT}), the atmospheric column, from either TOA (Top Of the Atmosphere) or the surface:

$$F_{IN} = LW^{\uparrow}_{SURF} + LW^{\downarrow}_{TOA} + LW^{\uparrow}_{LHF} + LW^{\uparrow}_{SHF} + SW^{\downarrow}_{TOA} + SW^{\uparrow}_{SURF}$$
$$F_{OUT} = LW^{\uparrow}_{TOA} + LW^{\downarrow}_{SURF} + SW^{\uparrow}_{TOA} + SW^{\downarrow}_{SURF}$$

Equation (6) is a pair of equations that we use to monitor radiative fluxes at both TOA (Nominal Top of Atmosphere) and SURF (Surface). The LHF (latent heat flux) and SHF (specific heat flux) at the surface is added since the RCE model specifically uses convective processes. Since this is purely a measure of energy in the system, we consider both the LW (Longwave) and SW (Shortwave) radiative frequencies and their distributions. As mentioned, we allow an error margin of 0.5 W/m^2 to account for minor disequilibrium. Therefore, the system is assumed to be at equilibrium and the time integration in the model is terminated if $|F_{IN} - F_{OUT}| < 0.5$.

Results

The results obtained after implementing the 0-d radiative model, 1-d radiative equilibrium model, and 1-d radiative-convective model are presented, analyzed, and discussed in this section. All models' estimations of outgoing longwave radiation (OLR) and surface temperature are compared to climatological normals (CNs) of the same. The 1-d models are then separately evaluated for their representation of the atmosphere.

Assessing the 0-d model performance involves a different approach than the one used for the 1-d models. Unlike its counterparts, it does not converge to a single surface temperature, instead providing a system of equations that can describe an equilibrium state at a range of temperatures. Because there are 3 variables being used in a single equation, we assume values for two and solve for the third. First, we evaluate the emissivity for realistic values of albedo and surface temperature. Borrowing from the climatologically-normal values of albedo and surface temperature chosen earlier, we estimate $\varepsilon = 0.619 \pm 4.25 \times 10^{-4}$ using Equation (1). The emissivity ratio here measures

the difference in the incoming and outgoing radiative fluxes in the system, and therefore acts as a correction factor. A value of unity for ε is more realistic since it represents the emissivity of the oceans which cover all of the surface of our aquaplanet.

Alternatively, using an ideal emissivity of 1, our predicted surface temperature falls to $T = 255.68\,K$ from a CN value of $T = 288.20 \pm 0.05\,K$. This calculation is made using the CN albedo value of 0.29 and the solar constant earlier mentioned to be 1367.6 W/m^2. We consider this value the 0-d's predicted surface temperature, given the realistic variable inputs. As expected, neither of the solutions described here are realistic.

Both of the 1-d models were designed to only terminate when OLR balanced out net solar flux at the top of the atmosphere within the previously-described error margin of 0.5 W/m^2. Therefore, the important variables to consider when evaluating the 1-d models are the surface temperature and air temperature profiles, instead of OLR. Both of the models make an improvement on the 0-d model, but it should be noted that the RCE model predicted a surface temperature far closer to the ideal CN.

Table 2. A comparison between model-estimated and observed (CN) OLR, surface temperature and planetary shortwave (SW) albedo values.

	OLR (W/m^2)	Surface Temperature (K)	Planetary Albedo
Climatological Normal (CN)	*234.17*	*288.20 ± 0.50*	*0.29*
Model 1 (0-d)	278.21 ± 2.21	255.68	-
Model 2 (1-d Radiative Equilibrium)	233.94	313.58	0.315
Model 3 (1-d RCE)	234.42	281.43	0.314

Atmospheric Profiles

Models 2 and 3 are also evaluated for their representations of their systems' atmospheric components. The 0-d model operates under a single-layer graybody assumption (caused by the addition of the emissivity ratio to the blackbody setup), maintaining internal vertical homogeneity. Therefore, relevant conclusions can only be drawn from the surface and at TOA, with intermediate levels yielding no significant results.

We use 4 key profiles to evaluate the equilibrium-state models' atmospheric profiles: shortwave and longwave radiative flux profiles, heating rates, and air temperature. We begin with Model 2 (radiative equilibrium), whose output is shown in Figure 2. Variables are plotted with respect to an inverted pressure (hPa) vertical coordinate. Note that air pressure is known to exponentially decrease with height.

We calculate the profile in (2a) as the difference between upwelling and downwelling shortwave fluxes. It is entirely negative since the net solar flux is downwelling. Its gradient demonstrates that most of the constituents affecting radiation in the shortwave are concentrated at higher pressures, since the attenuation primarily takes place past the 400 hPa pressure level. This makes sense given that the main shortwave absorber here is ozone. The low-altitude longwave absorption from carbon dioxide also explains Figure (2b)'s gradient. Since the net flux is upwelling, the range stays positive throughout the entire altitude shown here. Note that the flux divergence begins to converge to a value close to the OLR near the 150 hPa height, since very few CO_2 molecules exist to absorb longwave radiation at such low pressures.

The heating rates shown in Figure (2c) remain fairly high for this model. The low-altitude shortwave heating is countered by longwave cooling, resulting in a net radiative heating that is zero throughout the atmosphere. However this balance results in a temperature profile that is convective unstable - one of the drawbacks of the radiative equilibrium model being made evident here. We see two regions of unique significance here: below and above the 200 hPa pressure levels. The differences between the two are largely caused by ozone presence in the upper region.

The air temperature profile in Figure (2d) manifests the heating concerns hinted at in (2c). The lapse rate is fairly strong, exhibiting a 118 K drop in temperature across the lower region of the atmosphere. Consequently, the high lapse rates create an erroneously-high surface temperature, and an erroneously-low tropopause temperature. Therefore, a reasonable assumption would be that radiative transfer alone fails to transport enough energy upward from the surface to allow a lower-level profile close to observed values (which creates a 6.5K/km lapse rate in the troposphere). An additional cause for concern is the stark surface-air temperature gradient (~ 12 K between the surface and the first level of air for which temperature is measured) that would cause instability close to the surface. However, the upper-level profile appears far more accurate when compared to the lower-level profile, creating a far-more realistic temperature of 256 K at the 10 hPa pressure level.

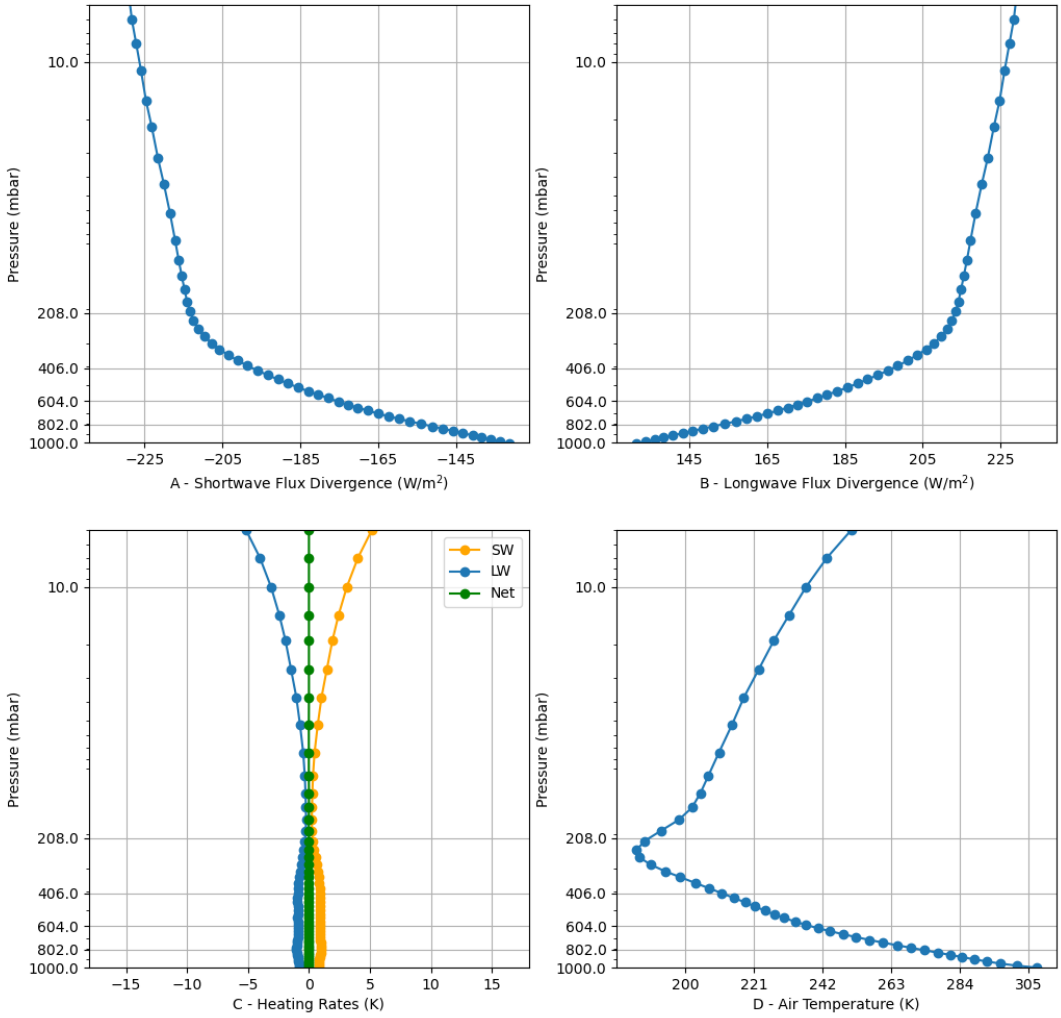

Figure 2. Output (vertical profiles) from the *1-d radiative equilibrium system (Model 2)* that quantifies the atmospheric component's equilibrium state. Figure 2(a) is a shortwave flux divergence (net flux) profile, Figure 2(b) is a longwave flux divergence profile, Figure 2(c) is a heating rate profile from both shortwave and longwave fluxes, and Figure 2(d) is the atmosphere's temperature profile.

We now move onto the RCE model. As expected, the shortwave flux profile in (3a) is similar to that in (2a). The longwave flux divergence profile exhibits a more controlled increase past the boundary layer. The increase in flux across the boundary layer is expected to be more substantial than in Model 2 given that it can only rely on radiative

transfer to transport energy from the surface to the atmosphere. The lower surface temperature implies that radiation emitted from lower altitudes is less than that in Model 2, which inevitably causes a greater increase in flux higher up in the atmosphere.

As mentioned, the boundary layer causes low-altitude net heating rates as shown in (3c) and convection results in net radiative heating rates being non-zero close to the surface. Thus, the lower part of the model is no longer in radiative equilibrium, and the balance is now between radiation, convection, and the boundary layer. The strong heating rates in the upper atmosphere match those in Model 2. A temperature inversion at the tropopause (caused by significant absorption of shortwave radiation due to ozone above this level) prevents the vertical exchange of air parcels required for convection. Therefore, Model 3 is expected to provide similar, if not identical results as Model 2 here.

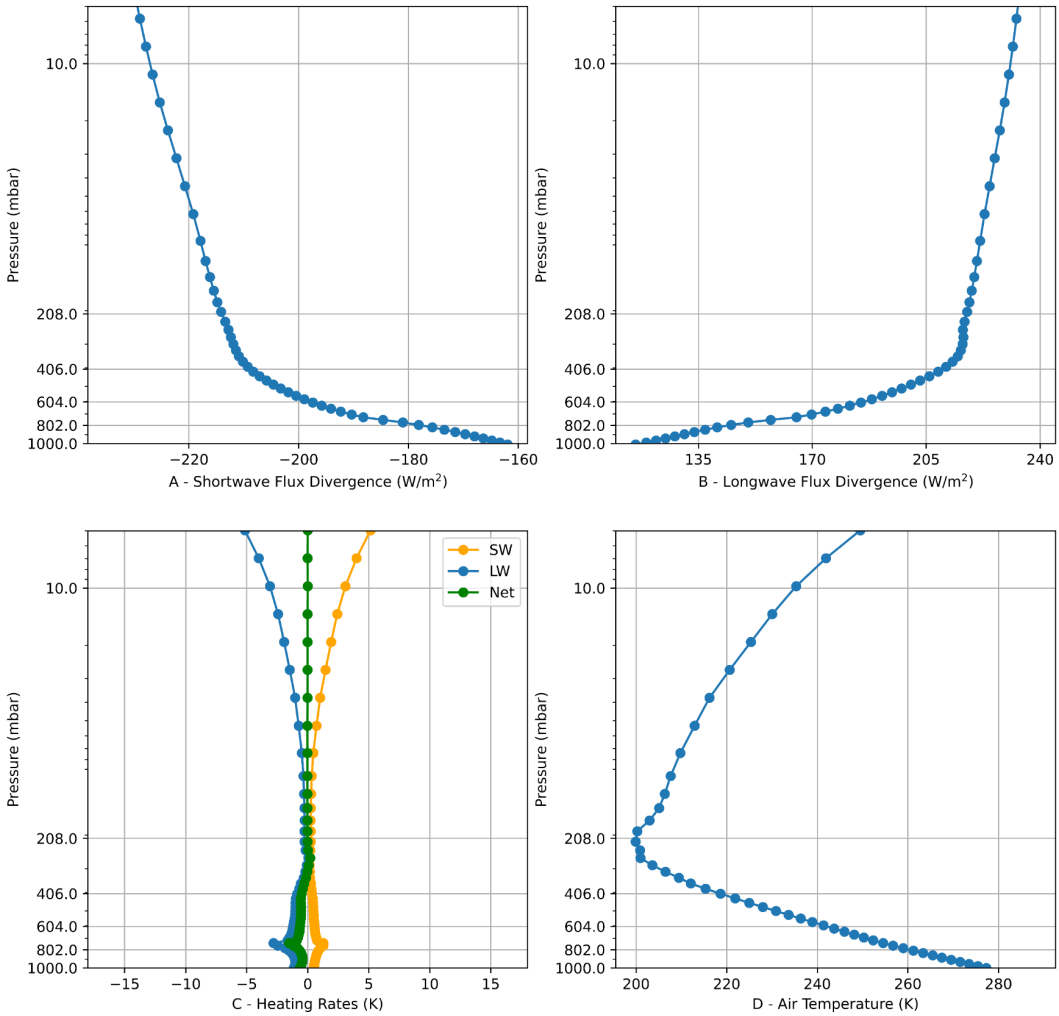

Figure 3. Output (vertical profiles) from the *1-d radiative-convective equilibrium system (Model 3)* that quantifies the atmospheric component's equilibrium state. Figure 3(a) is a shortwave flux divergence (net flux) profile, Figure 3(b) is a longwave flux divergence profile, Figure 3(c) is a heating rate profile from both shortwave and longwave fluxes, and Figure 3(d) is the atmosphere's temperature profile.

Figure (3d) shows an improvement on Model 2's air temperature profile. The restriction on radiation is manifested in the gradient from the surface to the 500 hPa pressure level. Given the exponential relationship between pressure and altitude, and the logarithmic scale on the y-axis, the constant gradient implies a maintenance of the

tropospheric lapse rate the convective adjustment seeks to maintain. This ensures that heat is transferred away from the surface, which creates a higher tropopause temperature and lower surface temperature. It also ensures that the surface-air temperature gradient is negligible (0.4 K), preventing the low-level radiative instability from Model 2. The effect of this controlled gradient is evidenced by the lowered drop in temperature across the troposphere (67 K).

Note that the stratospheric temperature profile in Models 2 and 3 are almost identical. The slightly-higher upper-level lapse rate in Model 2 is only caused by a lower temperature close to the ozone-induced inversion- which, in turn, is caused by the high low-level lapse rates that are a consequence of radiative equilibrium. Hence, we assume this difference would be further reduced by an identical temperature close to the inversion in Model 2.

Static Stability

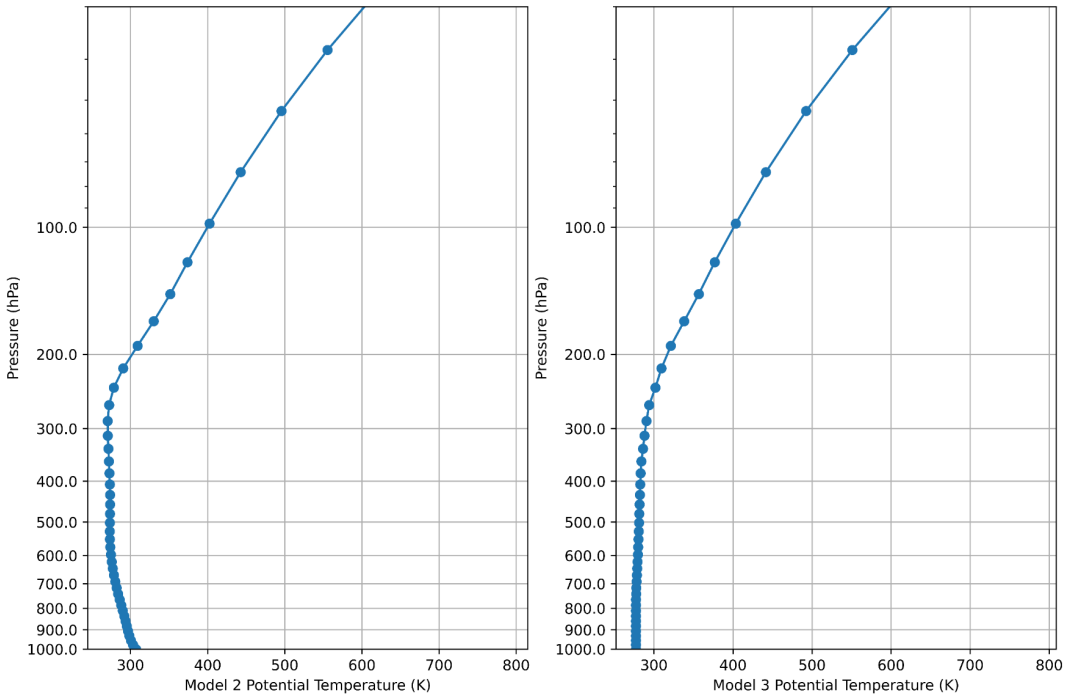

Figure 4. Potential temperature vertical profiles from Models 2 and 3.

An air mass is considered statically or convectively stable if it is able to resist any vertical displacement. We identify regions of static stability by analyzing the change in potential temperature with respect to height. Potential temperature is defined as the temperature an air parcel would gain if brought to a given pressure level adiabatically (without an exchange of heat between the parcel and the environment). We use MetPy's (May et. al., 2021) potential temperature function to calculate the profiles in Figure 3. For the atmosphere, the potential temperature is given by:

Equation 8: Potential temperature (Θ) as a function of air temperature and pressure.

$$\Theta(T,p) = T(\frac{p_0}{p})^{-R/c_p}$$

where $T$is the temperature of the parcel, $p_0$is the pressure at sea level, p is the pressure of the parcel, $R$is the gas constant, and c_p is the specific heat capacity of the gas.

The relationship between potential temperature and convective stability is well-established. If potential temperature were to decrease with height (i.e., $\partial\Theta/\partial z < 0$ or $\partial\Theta/\partial p > 0$), adiabatically-raised air parcels would be warmer than those at the same level. Being warmer than the surrounding environment, they will continue to rise further, resulting in an unstable atmosphere. Conversely, a statically stable atmosphere would show an increase in potential temperature with height ($\partial\Theta/\partial z > 0$ or $\partial\Theta/\partial p < 0$). An atmosphere with neutral static stability would exhibit roughly no change in potential temperature with height. In this case, any adiabatically displaced parcel would simply remain at the level to which it was displaced.

Both Models 2 and 3 exhibit similar upper-atmosphere potential temperature profiles, where potential temperature decreases with pressure (and thus, increases with height), as shown in Figure 3. As such, these regions are statically-stable and no vertical exchanges are expected to take place here. It should be noted that convection is actively suppressed here. This means that any instability that could be caused by a change in the amounts of certain non-transparent constituents could not be corrected using convective action.

However, their profiles begin to diverge near the surface. Model 2's low-altitude profile shows potential temperature falling with height. This creates static instability in the region, and would be subject to convection. However, the radiative equilibrium model does not include the physics of convection to correct the profile. Therefore, the low-level profile remains unstable even in the system's equilibrium state, as indicated earlier.

On the other hand, Model 3 exhibits a negligible change in potential temperature with height at these levels, implying neutral static stability in the region. This is because the convective instability induced by radiation that could be generated while running the model to equilibrium is removed by the convective component. Identifying statically stable and neutral regions of the Model 3 atmosphere allows us to clearly separate the tropopause from the stratosphere. Figure 4 indicates that the tropopause lies near the 200 hPa level. A similar distinction cannot be applied to Model 2 since the troposphere is defined as a region of convective activity.

Conclusion & Discussion

This paper's primary intention was to quantify, compare and evaluate the performances of 3 hierarchical commonly-used EBMs in order to identify the contexts in which each of them can be reasonably used. Given that they carry very different computational loads that generally increase with dimensional complexity and atmospheric constituency, an understanding of each of their forthcomings and strengths allow a user to optimize their choice between the three as per their requirements.

Our results show that Model 1 (0-d radiative equilibrium) is primarily suited to surfaces who have isothermal energy distributions. Since the two-stream approximations demonstrate that the position of an emitting layer plays a key role in optically-complex atmospheres, a 0-d graybody fails to model non-isothermal atmospheres. An isothermal energy distribution can be developed through a variety of methods. Planets that have a high surface heat capacity (e.g., aqua-planets) are likely to retain energy (without significant temperature changes) long enough to sidestep diurnal variations in insolation. Additionally, planets that have circulatory mechanisms capable of transferring heat in a manner efficient and rapid enough to create isothermal energy distributions can also be modeled using 0-d systems, albeit possibly with a gray coefficient. Similarly, planets with atmospheres sufficiently optically-thin that they can be disregarded may be modeled using 0-d techniques.

Model 2 (1-d radiative equilibrium) generally failed to model the tropospheric thermal profile, mainly due to the removal of the convective component and the insufficient surface-atmosphere energy transfer mechanisms. These inaccuracies manifested themselves in an erroneously-high surface temperature, and high temperature lapse rates -11.2 K/km in Model 2 as compared to 6.6 K/km in Model 3. However, the severity of these inaccuracies reduced as the atmosphere became convectively stable towards the upper layers of the atmosphere. This finding suggests that the model is likely to perform well in statically-stable sections of the atmosphere such as the Earth's stratosphere. Therefore, it improves on Model 1 by allowing planets with thermal variation along all spatial dimensions.

Model 3 (1-d RCE / radiative-convective equilibrium) was the best of the three. Its tropospheric profile is closer to the observed lapse rate ~ 6.5 K/km and suggests that radiation and convection are the primary 2 transfer mechanisms used in Earth's troposphere. However, the fact that Model 2 and 3 output similar stratospheric profiles suggests that convection is a negligible factor here, and may thus be modeled using radiative equilibrium. Therefore, radiative equilibrium models could be used in the presence of significant shortwave absorption throughout the atmosphere. The increased shortwave heating would balance out longwave cooling and cause a temperature lapse rate low enough such that the need for convection as a corrective mechanism is eliminated altogether.

Limitations & Further Study

Our choice in energy sources and sinks were made in the context of the Earth system alone. The elimination process described previously may not hold for other planets. The primary goal of the paper was to model the Earth system accurately enough to only inform us of the ideal contexts for the 3 techniques. Therefore, accuracy trade-offs were made to simplify this process. In particular, the 1-d model setups made large assumptions whose effects have not been evaluated here: a constant zenith angle (made necessary by the removal of x-y coordinates), no solar variability, an aquaplanet surface, an empirical shortwave albedo profile, etc. The 1-d models can be expanded in a variety of ways to test these effects: diurnal solar variation, the removal of the horizontal homogeneity assumption through the introduction of x-y dimensions, the consideration of other non-transparent atmospheric constituents (CFC, N_2O, etc.), further-optimized cloud parameterization, etc. Experiments similar to these papers' could be run with other planetary systems for which we have sufficient data to validate our conclusions.

Acknowledgements

I would like to express my gratitude to my advisor, Dr. Joy Merwin Monteiro, whose guidance has been instrumental in my exploration of climate modeling's importance, scope, and abilities. This article would not have been possible without his unwavering support and encouragement.

References

Monteiro, J. M., McGibbon, J., & Caballero, R. (2018). sympl (v. 0.4. 0) and climt (v. 0.15. 3)–towards a flexible framework for building model hierarchies in Python. *Geoscientific Model Development*, *11*(9), 3781-3794. https://do i.org/10.5194/gmd-11-3781-2018

Durran, D. R. (1991). The third-order Adams-Bashforth method: An attractive alternative to leapfrog time differencing. *Monthly weather review*, *119*(3), 702-720. https://doi.org/10.1175/1520-0493(1991)119%3C0702:TTOABM%3E2.0.CO;2

Dasgupta, M. (2021). Mihir-DG/earth-EBMs. https://github.com/Mihir-DG/earth-EBMs

McNaught, A. D. (1997). *Compendium of chemical terminology* (Vol. 1669). Oxford: Blackwell Science. https://www.old.iupac.org/publications/books/author/mcnaught.html

Manabe, S., & Wetherald, R. T. (1967). Thermal equilibrium of the atmosphere with a given distribution of relative humidity. https://doi.org/10.1175/1520-0469(1967)024%3C0241:TEOTAW%3E2.0.CO;2

Stephens, G. L., O'Brien, D., Webster, P. J., Pilewski, P., Kato, S., & Li, J. L. (2015). The albedo of Earth. *Reviews of geophysics*, *53*(1), 141-163. https://doi.org/10.1002/2014RG000449

Wielicki, B. A., Barkstrom, B. R., Harrison, E. F., Lee III, R. B., Smith, G. L., & Cooper, J. E. (1996). Clouds and the Earth's Radiant Energy System (CERES): An earth observing system experiment. *Bulletin of the American Meteorological Society*, *77*(5), 853-868. https://doi.org/10.1175/1520-0477(1996)077%3C0853:CATERE%3E2.0. CO;2

Jacobowitz, H., & Tighe, R. J. (1984). The earth radiation budget derived from the NIMBUS 7 ERB experiment. *Journal of Geophysical Research: Atmospheres*, *89*(D4), 4997-5010. https://doi.org/10.1029/JD089iD04p04997

Greene, T., Jacobs, P., NASA Release 21-005, 2021. 2020 Tied for Warmest Year on Record, NASA Analysis Shows. https://www.giss.nasa.gov/research/news/20210114/

Hansen, J., Ruedy, R., Sato, M., & Lo, K. (2010). Global surface temperature change. *Reviews of Geophysics*, *48*(4). https://doi.org/10.1029/2010RG000345

Lenssen, N. J., Schmidt, G. A., Hansen, J. E., Menne, M. J., Persin, A., Ruedy, R., & Zyss, D. (2019). Improvements in the GISTEMP uncertainty model. *Journal of Geophysical Research: Atmospheres*, *124*(12), 6307-6326. https://doi.org/10.1029/2018JD029522

Liebmann, B., & Smith, C. A. (1996). Description of a complete (interpolated) outgoing longwave radiation dataset. *Bulletin of the American Meteorological Society*, *77*(6), 1275-1277. https://psl.noaa.gov/data/gridded/data. interp_OLR.html

Hersbach, H., Bell, B., Berrisford, P., Hirahara, S., Horányi, A., Muñoz-Sabater, J., ... & Thépaut, J. N. (2020). The ERA5 global reanalysis. *Quarterly Journal of the Royal Meteorological Society*, *146*(730), 1999-2049. https://doi.org/10.1002/qj.3803

Kobayashi, S., Ota, Y., Harada, Y., Ebita, A., Moriya, M., Onoda, H., ... & Takahashi, K. (2015). The JRA-55 reanalysis: General specifications and basic characteristics. *Journal of the Meteorological Society of Japan. Ser. II*, *93*(1), 5-48. https://doi.org/10.2151/jmsj.2015-001

Gelaro, R., McCarty, W., Suárez, M. J., Todling, R., Molod, A., Takacs, L., ... & Zhao, B. (2017). The modern-era retrospective analysis for research and applications, version 2 (MERRA-2). *Journal of climate*, *30*(14), 5419-5454. https://doi.org/10.1175/JCLI-D-16-0758.1

Kalnay, E., Kanamitsu, M., Kistler, R., Collins, W., Deaven, D., Gandin, L., ... & Joseph, D. (1996). The NCEP/NCAR 40-year reanalysis project. *Bulletin of the American meteorological Society*, *77*(3), 437-472. https:// doi.org /10.1175/1520-0477(1996)077%3C0437:TNYRP%3E2.0.CO;2

Ernst, W. G., Sleep, N. H., & Tsujimori, T. (2016). Plate-tectonic evolution of the Earth: bottom-up and top-down mantle circulation. *Canadian Journal of Earth Sciences*, *53*(11), 1103-1120. https://doi.org/10.1139/cjes-2015-0126

Camuffo, D. (2001). Lunar influences on climate. In *Earth-Moon Relationships* (pp. 99-113). Springer, Dordrecht. ht tp://dx.doi.org/10.1023/A:1017099427908

Lenardic, A., Moresi, L. N., Jellinek, A. M., & Manga, M. (2005). Continental insulation, mantle cooling, and the surface area of oceans and continents. *Earth and Planetary Science Letters*, *234*(3-4), 317-333. https://doi.org/10 .1016/j.epsl.2005.01.038

Johnson, F. S. (1954). The solar constant. *Journal of Atmospheric Sciences*, *11*(6), 431-439. https://doi.org/10.1175/1520-0469(1954)011%3C0431:TSC%3E2.0.CO;2

Meador, W. E., & Weaver, W. R. (1980). Two-stream approximations to radiative transfer in planetary atmospheres: A unified description of existing methods and a new improvement. *Journal of Atmospheric Sciences*, *37*(3), 630-643. https://doi.org/10.1175/1520-0469(1980)037%3C0630:TSATRT%3E2.0.CO;2

Catling, D. C., & Zahnle, K. J. (2009). The planetary air leak. *Scientific American*, *300*(5), 36-43 http://faculty.washington.edu/dcatling/Catling2009_SciAm.pdf

Mlawer, E. J., Taubman, S. J., Brown, P. D., Iacono, M. J., & Clough, S. A. (1997). Radiative transfer for inhomogeneous atmospheres: RRTM, a validated correlated-k model for the longwave. *Journal of Geophysical Research: Atmospheres*, *102*(D14), 16663-16682. https://doi.org/10.1029/97JD00237

Emanuel, K. A., & Živković-Rothman, M. (1999). Development and evaluation of a convection scheme for use in climate models. *Journal of the Atmospheric Sciences*, *56*(11), 1766-1782. https://doi.org/10.1175/1520-0469(1999)056%3C1766:DAEOAC%3E2.0.CO;2

May, R. M., Arms, S. C., Marsh, P., Bruning, E., Leeman, J. R., Goebbert, K., Thielen, J. E., Bruick, Z., and Camron, M. D., 2021: MetPy: A Python Package for Meteorological Data. Unidata. https://github.com/Unidata/MetPy, https://doi.org/10.5065/D6WW7G29.